

ARTICLE

Open Access

Accordion-like plasmonic silver nanorod array exhibiting multiple electromagnetic responses

Mooseong Kim¹, Jungho Mun², Dusik Bae¹, Gumhye Jeon¹, Myeong Cheol Go¹, Junsuk Rho^{1,2,3} and Jin Kon Kim¹

Abstract

We prepared a high-density array of “accordion-like” plasmonic silver nanorods over a large area ($2.5 \times 2.5 \text{ cm}^2$) that exhibited multiple electromagnetic responses to visible and near-infrared (NIR) wavelengths. This array of “accordion-like” silver nanorods was fabricated by confining the lamellae-forming polystyrene-*block*-poly (methyl methacrylate) copolymer (PS-*b*-PMMA) inside the cylindrical pores of an aluminum oxide (AAO) template grafted with thin neutral brush layers. PS and PMMA lamellar nanodomains with sizes of 15 nm were alternatively stacked along the nanorod direction. After the AAO template was removed, a 5-nm-thick layer of silver was thermally deposited on only the PS nanodomains. Owing to the multiple resonances exhibited in the visible and NIR regimes, the array could be used for multi-analyte detection. Furthermore, this concept of fabricating sophisticated nanoscale architectures by utilizing block copolymer self-assembly and incorporating plasmonic metals into one nanodomain could be applied to realize large-scale metamaterials that function under visible and NIR wavelengths.

Introduction

Plasmonics has achieved many unique optical properties by exploiting the surface plasmon polaritons, or the collective oscillation of free charges strongly coupled to light, that exhibit subwavelength modes with extremely enhanced electric field intensities^{1–3}. Taking advantage of such properties, two-dimensional ensembles of plasmonic nanostructures have been arranged for surface-enhanced Raman scattering substrates^{4–6}, metamaterials^{7–9}, and nonlinear optics^{10,11}. The localized surface plasmon resonance strongly depends on the structural geometry, and a variety of optical properties have been realized by metallic nanostructures^{12,13}.

One of the most interesting applications of nano-plasmonics is the fundamental control of the electromagnetic properties by using a metamaterial. This effectively homogeneous material has demonstrated many extraordinary optical properties, such as artificial magnetism^{14–16}, a negative refractive index^{17–20}, strong artificial optical activity^{21,22}, and perfect absorption^{23–26}. However, the realization of these properties often requires a magnetic response that is introduced through the fabrication of complex three-dimensional (3D) architectures, for instance, split-ring resonators²⁷, core shells^{28,29}, and vertically stacked rods³⁰. Well-defined complex nanostructures with a magnetic response are usually prepared by top-down approaches, including direct laser writing³¹, multiple e-beam lithography³², and membrane projection lithography³³. Gansel et al.³⁴ achieved broadband circular dichroism in a gold helix photonic metamaterial fabricated through direct-write 3D laser lithography, but the operating window of this material was limited to the near-infrared (NIR) regime due to its large feature size (2 μm). Liu et al.³⁵

Correspondence: Junsuk Rho (jsrho@postech.ac.kr) or Jin Kon Kim (jkkim@postech.ac.kr)

¹National Creative Research Initiative Center for Block Copolymer Self-Assembly, Department of Chemical Engineering, Pohang University of Science and Technology (POSTECH), Pohang, Gyeongbuk 37673, Republic of Korea

²Department of Chemical Engineering, Pohang University of Science and Technology (POSTECH), Pohang, Gyeongbuk 37673, Republic of Korea

Full list of author information is available at the end of the article

These authors contributed equally: Mooseong Kim, Jungho Mun.

© The Author(s) 2018



Open Access This article is licensed under a Creative Commons Attribution 4.0 International License, which permits use, sharing, adaptation, distribution and reproduction in any medium or format, as long as you give appropriate credit to the original author(s) and the source, provide a link to the Creative Commons license, and indicate if changes were made. The images or other third party material in this article are included in the article's Creative Commons license, unless indicated otherwise in a credit line to the material. If material is not included in the article's Creative Commons license and your intended use is not permitted by statutory regulation or exceeds the permitted use, you will need to obtain permission directly from the copyright holder. To view a copy of this license, visit <http://creativecommons.org/licenses/by/4.0/>.

demonstrated a negative permeability with a stack of four split-ring resonators fabricated through multiple e-beam lithography, but large-scale device fabrication of this structure is practically impossible.

The realistic application of plasmonic metamaterials with complex geometries requires large-area fabrication and feature sizes below 100 nm to have a working regime of visible to NIR wavelengths. The bottom-up approach, particularly the self-assembly of a block copolymer (BCP), could satisfy these two requirements for the fabrication of complex plasmonic nanostructures over a large area^{36–38}. BCPs self-assemble into various nanodomains, such as lamellae, gyroids, cylinders, and spheres, depending on the volume fraction of each block³⁹. Although these nanodomains in their bulk states do not align to form complex nanostructures, the confinement of nanodomains inside a constrained geometry can provide uncommon architectures, such as single⁴⁰ and double helices⁴¹ and toroid shapes⁴², that have not been observed in the bulk state. Anodized aluminum oxide (AAO) templates with tunable sub-100 nm pore sizes have been widely applied in the preparation of bulk metamaterials^{43,44}. Here we combined BCP self-assembly and an AAO template to form a unique complex nanostructure. We focused on stacked lamellar nanostructures⁴⁵, where each nanodomain is alternatively stacked along the direction of the nanorod.

This paper demonstrates the fabrication of sophisticated nanostructures that are difficult to realize through the top-down process in a large optical device by taking advantage of BCP self-assembly. Specifically, we fabricated a high-density array of 3D plasmonic nanostructures on the centimeter scale through the confinement of lamellar nanodomains of BCP inside the cylindrical pores of an AAO template. This confinement allowed us to obtain a vertically stacked lamellar nanostructure. Once Ag was deposited on only one of the two nanodomains, a high-density array of “accordion-like” Ag nanorods was fabricated over a large area. This array shows three transmittance dips, the origins of which are explained through finite-difference time-domain (FDTD) simulations. The retrieved effective electromagnetic properties and the corresponding field patterns reveal multiple electromagnetic responses in the visible-NIR regime and their

origins. Owing to these multiple modes, which include both magnetic and electric responses, this bottom-up approach based on the confinement of BCP nanodomains could be applied to the development of metamaterials for multi-analyte sensing^{46–48}, imaging^{49,50}, and invisibility cloaking^{51–55}.

Materials and methods

Chemicals and AAO fabrication

PS-*b*-PMMA (SML-51) and PS-*ran*-PMMA-OH were purchased from Polymer Source Inc, (Quebec, Canada) and used as received (Table 1). Epoxy resin (Araldite resin grade 502: (50:45:5 wt/wt/wt) dodecylsuccinic anhydride:phenol,2,4,6-tris[(dimethylamino) methyl]-[90-72-2]:bis(dimethylaminomethyl) phenol) was purchased from Polymer Source Inc. The AAO template was prepared by the well-established two-step anodization method⁵⁶. The first anodization step was performed in an aqueous oxalic acid solution to obtain the perfect hexagonal pore arrangement over a large area. The center-to-center distance between two neighboring pores in this AAO membrane was 100 nm. After the irregular pores in the AAO were removed, the second anodization step was performed for 120 s. The pore diameter was controlled by adjusting the pore-widening time in a 0.1 M H₃PO₄ aqueous solution at 30 °C (see Sec. S1 of the SI).

Fabrication of a high-density array of accordion-like nanorods

First, PS-*ran*-PMMA-OH solutions in toluene (0.5 wt % in solid) were dropped on an AAO template and annealed at 180 °C for 3 days under vacuum. The non-grafted PS-*ran*-PMMA-OH chains were completely removed by rinsing with toluene. This treatment made the AAO pore walls neutral to both PS and PMMA chains (Fig. 1a). Then SML-51 in toluene (2 wt%) was spin-coated on the AAO template and annealed at 200 °C for 3 days in vacuum, followed by quenching to room temperature. Epoxy resin (with a thickness of 0.5 mm) was dropped on the as-annealed AAO template and cured at 60 °C for 12 h (Fig. 1b). Next, the aluminum layer on the AAO template was removed by using a CuCl₂ solution (9 g of CuCl₂, 20 mL of 0.1 M HCl, 100

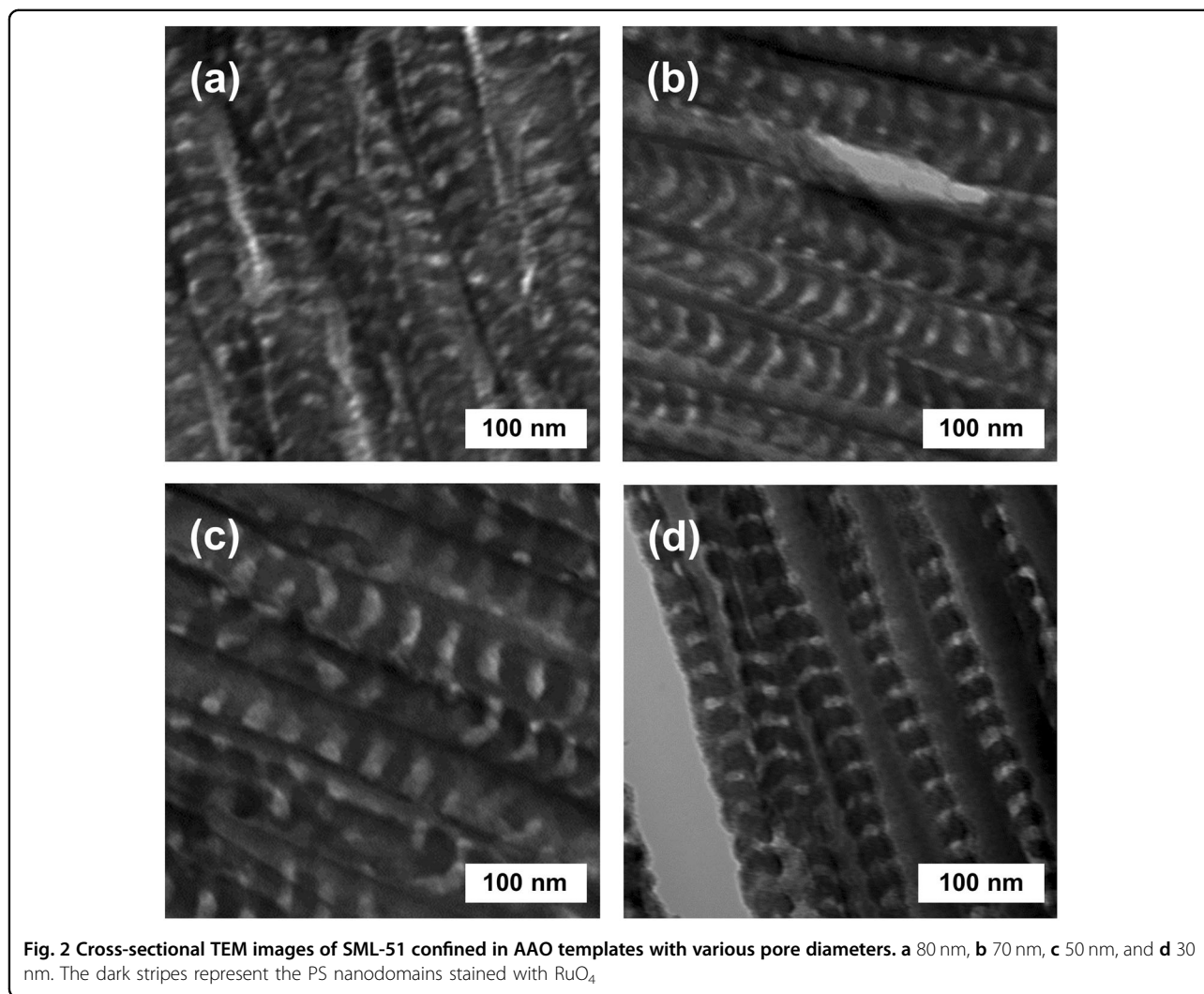
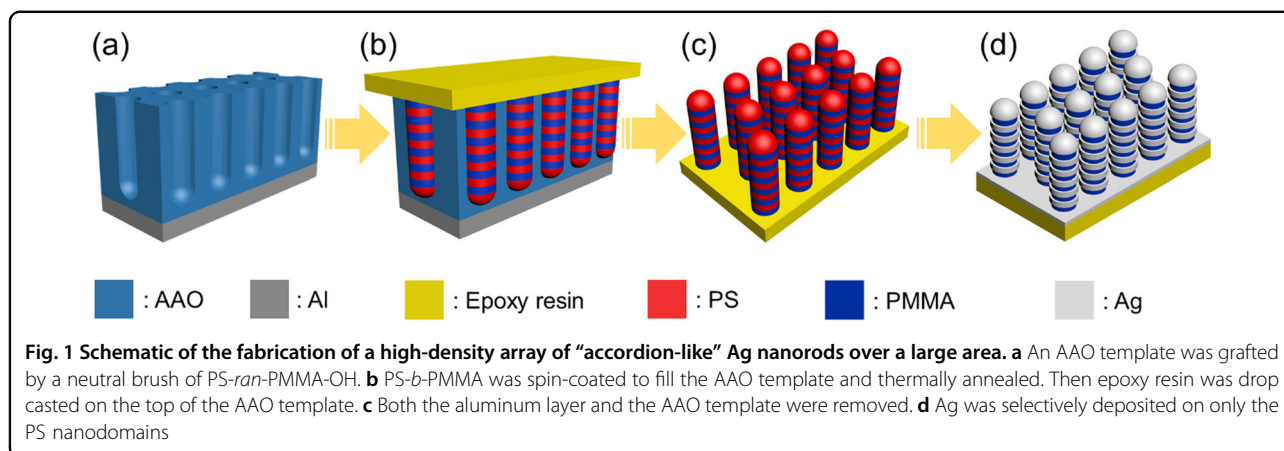
Table 1 Molecular characteristics of SML-51, PS-*ran*-PMMA, and PS homopolymer

| Polymer | Lot no. (supplier) | M_n [kg mol ⁻¹] | M_w/M_n^a | L_0^b [nm] | f_{PS}^c |
|-------------------------|-------------------------|-------------------------------|-------------|--------------|------------|
| SML-51 | P4961 (Polymer Source) | 51 | 1.06 | 32.9 | 0.52 |
| PS- <i>ran</i> -PMMA-OH | P6469A (Polymer Source) | 7 | 1.48 | | 0.57 |

^a M_n and M_w are the number and weight average molecular weights, respectively

^b The lamellar domain spacing measured by small-angle X-ray scattering

^c Volume fraction of the PS block measured by ¹H NMR and the known densities of PS (1.04 g cm⁻³) and PMMA (1.18 g cm⁻³)



mL of DI water), and the AAO template was removed by using a 0.4 M sodium hydroxide aqueous solution for 120 min (Fig. 1c). Finally, 5-nm-thick Ag was selectively

deposited on the PS nanodomains of all the nanorods by thermal evaporation⁵⁷ at a rate of 0.01 nm s⁻¹ under high vacuum (Fig. 1d).

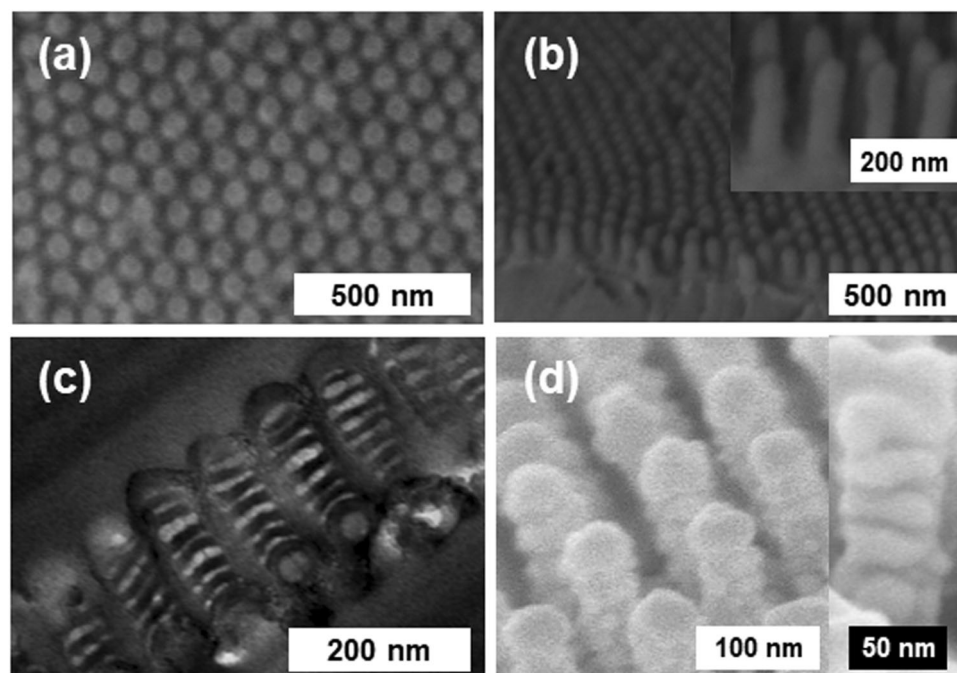


Fig. 3 FE-SEM images of the PS-*b*-PMMA nanorods. **a** Top and **(b)** 80°-tilted side views (the inset is an enlarged image) after removal of the AAO template. **c** Cross-sectional TEM image showing the inner stacked lamellae in the nanorods. **d** 80°-tilted view SEM image showing the Ag accordion nanostructure

The arrangement of the PS-*b*-PMMA nanodomains confined in the AAO template was examined via transmission electron microscopy (TEM; S-7600: Hitachi Ltd., operating at an accelerating voltage of 80 kV). To make a sample for the TEM, epoxy resin was first embedded on the AAO template containing PS-*b*-PMMA. After removal of the aluminum and AAO template, epoxy resin was again dropped on the array of PS-*b*-PMMA nanorods and cured. After ultrathin sections were prepared using a Leica Ultracut Microtome (EM UC6 Leica Ltd.) equipped with a diamond knife, the samples were stained with ruthenium tetroxide (RuO₄), a staining agent selective for the PS nanodomains. The vertical alignment of the nanorods on the epoxy substrate after removing the AAO template was examined via field emission scanning electron microscopy (FE-SEM; Hitachi S-4800). Transmittance spectra were measured via an Fourier transform-infrared spectrometer (Bruker Vertex 70) equipped with a microscope (Bruker Hyperion 2000).

FDTD simulations

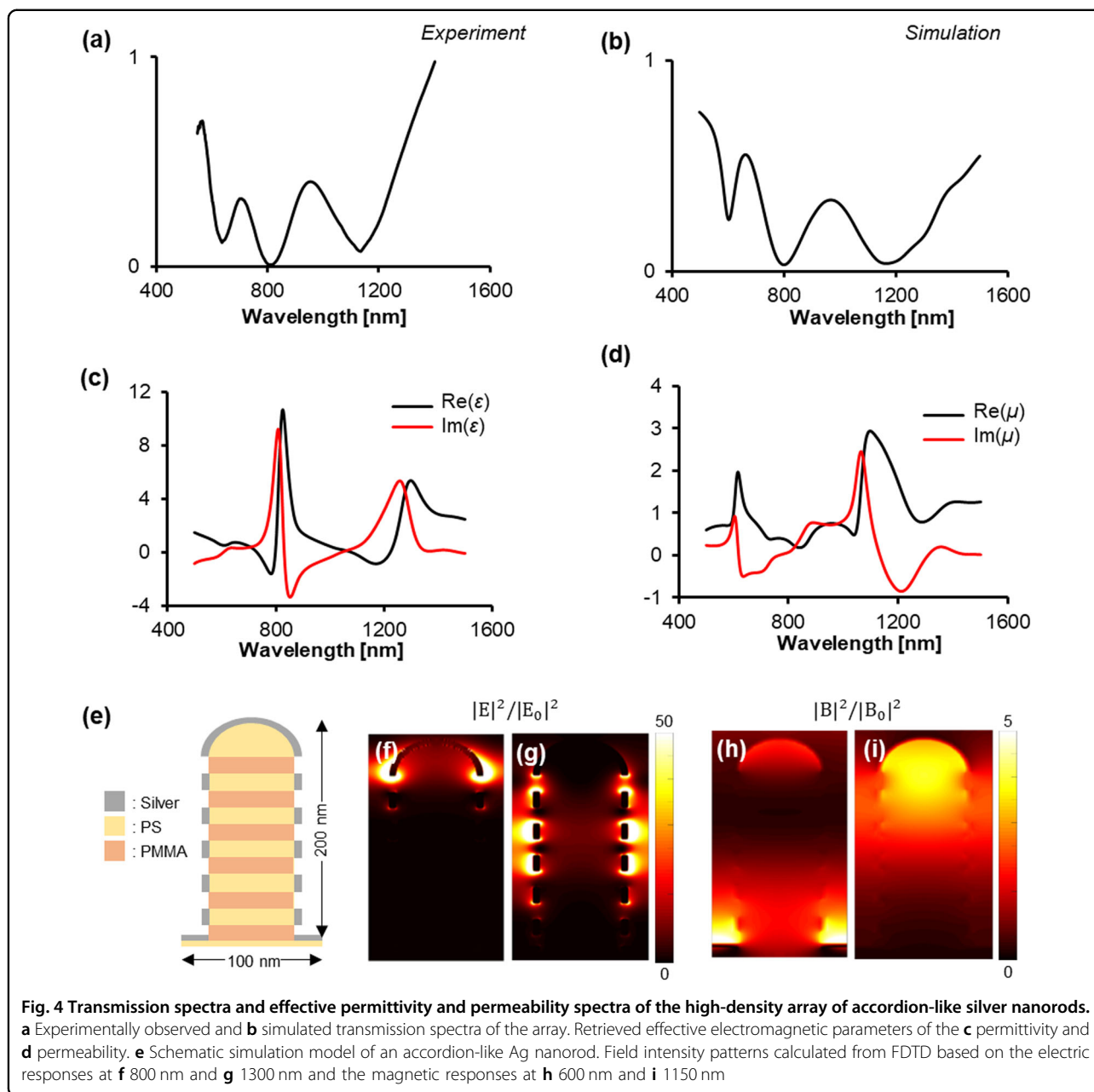
3D full-wave numerical simulations were conducted to analyze the electromagnetic properties of the hexagonally packed Ag accordion nanorod array. A commercial-grade simulator (Lumerical) based on the FDTD method was used to calculate the electromagnetic field. The simulation model was designed by

SEM/TEM observations (see Sec. S2 of the SI), and the simulation mesh size was set to <0.3 nm to account for the small feature size. The electromagnetic field was calculated with polarized incident light. The refractive index of PS-*b*-PMMA and the epoxy resin was 1.53, as measured using ellipsometry, and the Ag permittivity was taken from Johnson and Christy⁵⁸.

Results

Morphology

The versatile tunability of the AAO template is illustrated in the cross-sectional TEM images of SML-51 confined in AAO templates with various pore diameters ranging from 30 to 80 nm (Fig. 2). Alternatingly stacked lamellae of PS and PMMA nanodomains are clearly observed in the TEM images independent of the AAO pore diameter. In general, the PS and PMMA nanodomains on a flat surface are vertically oriented when treated by a neutral brush⁵⁹. Although the substrate (the AAO wall) in this study was not flat, the neutrality of the AAO walls allowed the PS and PMMA chains to align well along the wall. While the vertical orientation of the lamellae-forming PS-*b*-PMMA was achieved on a flat surface with the neutral brush for a range of film thicknesses (H) ($0.3-1.4 H/L_0$)⁵⁹, stacked lamellae are observed inside the AAO for D/L_0 values between 0.91 and 2.31 (D is the diameter of the AAO pore).



A high-density array of vertically oriented nanorods was successfully fabricated over a large area ($2.5 \times 2.5 \text{ cm}^2$) (see Sec. S3 of SI), and the BCP nanorods were clearly observed by removing the AAO template (Fig. 3a, b). PS and PMMA nanodomains are alternatively stacked along the nanorod direction (Fig. 3c). Thermal evaporation of Ag onto the array resulted in the deposition of Ag on only the PS nanodomains (Fig. 3d). This selective deposition comes from the higher affinity of Ag for PS than the PMMA nanodomains^{57,60}. Based on the SEM images, the center-to-center distance of the Ag stripes was determined to be

30 nm, which is consistent with the L_0 of PS-*b*-PMMA (32.9 nm). Thus a high-density array of “accordion-like” Ag nanorods were successfully fabricated over a large area.

Optical properties and FDTD simulations

The high-density array of accordion-like Ag nanorods exhibited three transmittance (T) dips at 600, 800, and 1200 nm (Fig. 4a), while an array of PS nanorods with uniformly deposited (not accordion-shaped) Ag showed only one dip at 450 nm (see Sec. S5 of the SI). This result indicates that the multiple T dips result from the

accordion-like shape of the nanorods with periodic Ag side rings that are vertically displaced by the lamella thickness of the PMMA block in SML-51. The simulated FDTD results (Fig. 4b) show three T dips at positions that are consistent with the experimentally measured spectra. This consistency in the experimental and simulated T spectra allows us to proceed to calculate the effective electromagnetic parameters of the array (Fig. 4c, d). The major T dips at 800 and 1200 nm correspond to electric responses (Fig. 4c), while the other dip at 600 nm corresponds to a magnetic response (Fig. 4d). The other magnetic response at 1150 nm could not produce a T dip, possibly due to its spectral closeness to the electric response at 1300 nm, which compensates for the effect on the wave impedance (see Sec. S4.2 of the SI).

The origin of each response was analyzed from the corresponding electromagnetic field patterns of the Ag accordion nanostructure. Here we consider each nanorod to have five Ag rings and one hemispherical cover (Fig. 4e) to mimic the experimentally observed accordion-like Ag nanorod (Fig. 3d). The strong electric response at 800 nm arises from the Ag hemispherical cover (Fig. 4f). The weaker electric response at approximately 1300 nm results from the Ag side rings (Fig. 4g). These two electric responses are enhanced through coupling between neighboring nanorods in the high-density array. The magnetic response at 600 nm arises from the plasmonic mode of the continuous Ag film deposited on the substrate (Fig. 4h). Another magnetic response at 1150 nm comes from the Ag hemisphere cover. This result is particularly interesting since the Ag hemisphere itself, without Ag side rings, does not exhibit any magnetic response at this wavelength (see case (5) in Fig. S6 of the SI). Thus the magnetic response possibly arises from the current loop along the hemisphere driven by the electric response of the Ag side rings. This result shows that the magnetic response of a nanostructure (i.e., a Ag hemisphere) could be induced by a nearby resonant structure (i.e., Ag side rings). The effect of each component in a single accordion-like nanorod on the electric and magnetic responses is discussed in detail in Sec. S6 of the SI. Finally, the size effect of the nanorods, for instance, the radius and height of the nanorod and the vertical gap distance, which could be tuned by altering the AAO template and the molecular weight of the BCP, on the electromagnetic responses is discussed in Sec. S7 of the SI.

Conclusion

In summary, a high-density array of accordion-like plasmonic Ag nanorods was successfully fabricated over a large area ($\sim\text{cm}^2$) by confining lamellar nanodomains inside cylindrical AAO pores. The array showed multiple electromagnetic responses to visible and NIR wavelengths.

Through FDTD simulations, the T dip at 600 nm was determined to correspond to a magnetic response, while the other T dips at 800 and 1200 nm corresponded to electric responses. Interestingly, a magnetic response at 1150 nm arose from the hemispherical cover of the nanorods. Although this hemisphere alone did not show a magnetic response at this wavelength, a magnetic response was induced by the electric resonance of the Ag side rings. This coupling between the two different structures at different resonant wavelengths could be used to engineer a metamaterial with a desired magnetic response to visible and NIR wavelengths. This realization of multiple responses in complex nanostructures through BCP self-assembly may pave the way for various practical applications, such as multi-analyte detection, and metamaterials with unique optical properties, such as a negative refractive index.

Acknowledgements

J.K.K. acknowledges financial support from the National Creative Research Initiative Program (2013R1A3A2042196), and J.R. acknowledges the National Research Foundation of Korea grants (2017R1E1A2A01076613, 2017R1E1A1A03070501, NRF-2015R1A5A1037668, and CAMM-2014M3A6B3063708).

Author details

¹National Creative Research Initiative Center for Block Copolymer Self-Assembly, Department of Chemical Engineering, Pohang University of Science and Technology (POSTECH), Pohang, Gyeongbuk 37673, Republic of Korea. ²Department of Chemical Engineering, Pohang University of Science and Technology (POSTECH), Pohang, Gyeongbuk 37673, Republic of Korea. ³Department of Mechanical Engineering, Pohang University of Science and Technology (POSTECH), Pohang, Gyeongbuk 37673, Republic of Korea

Conflict of interest

The authors declare that they have no conflict of interest.

Publisher's note

Springer Nature remains neutral with regard to jurisdictional claims in published maps and institutional affiliations.

Supplementary information is available for this paper at <https://doi.org/10.1038/s41427-018-0033-6>.

Received: 27 October 2017 Revised: 12 January 2018 Accepted: 7 February 2018.

Published online: 11 April 2018

References

1. Jones, M. R., Osberg, K. D., Macfarlane, R. J., Langille, M. R. & Mirkin, C. A. Templated techniques for the synthesis and assembly of plasmonic nanostructures. *Chem. Rev.* **111**, 3736–3827 (2011).
2. Tan, S. J., Campolongo, M. J., Luo, D. & Cheng, W. Building plasmonic nanostructures with DNA. *Nat. Nanotechnol.* **6**, 268–276 (2011).
3. Dintinger, J., Muhlig, S., Rockstuhl, C. & Scharf, T. A bottom-up approach to fabricate optical metamaterials by self-assembled metallic nanoparticles. *Opt. Mater. Express* **2**, 269–278 (2012).
4. Chen, Y. et al. Ultrathin plasmene nanosheets as soft and surface-attachable SERS substrates with high signal uniformity. *Adv. Opt. Mater.* **3**, 919–924 (2015).
5. Si, K. J., Guo, P., Shi, Q. & Cheng, W. Self-assembled nanocube-based plasmene nanosheets as soft surface-enhanced Raman scattering substrates toward direct quantitative drug identification on surfaces. *Anal. Chem.* **87**, 5263–5269 (2015).

6. Cho, W. J., Kim, Y. & Kim, J. K. Ultrahigh-density array of silver nanoclusters for SERS substrate with high sensitivity and excellent reproducibility. *ACS Nano* **6**, 249–255 (2011).
7. Yao, K. & Liu, Y. Plasmonic metamaterials. *Nanotechnol. Rev.* **3**, 177–210 (2014).
8. Morgan, F., Murphy, A., Hendren, W., Wurtz, G. & Pollard, R. J. In-situ ellipsometric monitoring of gold nanorod metamaterials growth. *ACS Appl. Mater. Interfaces* **9**, 17379–17386 (2017).
9. McPhedran, R. C., Shadrivov, I. V., Kuhlmeiy, B. T. & Kivshar, Y. S. Metamaterials and metaoptics. *NPG Asia Mater.* **3**, 100–108 (2011).
10. Kauranen, M. & Zayats, A. V. Nonlinear plasmonics. *Nat. Photonics* **6**, 737–748 (2012).
11. Yang, Y. et al. Hyperbolic spoof plasmonic metasurfaces. *NPG Asia Mater.* **9**, e428 (2017).
12. Noguez, C. Surface plasmons on metal nanoparticles: the influence of shape and physical environment. *J. Phys. Chem. C* **111**, 3806–3819 (2007).
13. Wei, T. et al. Surface-dependent localized surface plasmon resonances in CuS nanodisks. *ACS Appl. Mater. Interfaces* **5**, 10473–10477 (2013).
14. Pendry, J. B., Holden, A. J., Robbins, D. & Stewart, W. Magnetism from conductors and enhanced nonlinear phenomena. *IEEE Trans. Microw. Theory Tech.* **47**, 2075–2084 (1999).
15. Verre, R., Yang, Z.-J., Shegai, T. & Kall, M. Optical magnetism and plasmonic Fano resonances in metal–insulator–metal oligomers. *Nano Lett.* **15**, 1952–1958 (2015).
16. Susman, M. D., Vaskevich, A. & Rubinstein, I. Refractive index sensing using visible electromagnetic resonances of supported Cu₂O particles. *ACS Appl. Mater. Interfaces* **9**, 8177–8186 (2017).
17. Shelby, R. A., Smith, D. R. & Schultz, S. Experimental verification of a negative index of refraction. *Science* **292**, 77–79 (2001).
18. Smith, D. R., Pendry, J. B. & Wiltshire, M. C. Metamaterials and negative refractive index. *Science* **305**, 788–792 (2004).
19. Shalaev, V. M. Optical negative-index metamaterials. *Nat. Photonics* **1**, 41–48 (2007).
20. Soukoulis, C. M., Kafesaki, M. & Economou, E. N. Negative-index materials: new frontiers in optics. *Adv. Mater.* **18**, 1941–1952 (2006).
21. Decker, M., Klein, M., Wegener, M. & Linden, S. Circular dichroism of planar chiral magnetic metamaterials. *Opt. Lett.* **32**, 856–858 (2007).
22. Li, Z., Mutlu, M. & Ozbay, E. Chiral metamaterials: from optical activity and negative refractive index to asymmetric transmission. *J. Opt.* **15**, 023001 (2013).
23. Cui, Y. et al. Ultrabroadband light absorption by a sawtooth anisotropic metamaterial slab. *Nano Lett.* **12**, 1443–1447 (2012).
24. Watts, C. M., Liu, X. & Padilla, W. J. Metamaterial electromagnetic wave absorbers. *Adv. Mater.* **24**, OP98–120, OP181 (2012).
25. Landy, N. I., Sajuyigbe, S., Mock, J., Smith, D. & Padilla, W. Perfect metamaterial absorber. *Phys. Rev. Lett.* **100**, 207402 (2008).
26. Akselrod, G. M. et al. Large-area metasurface perfect absorbers from visible to near-infrared. *Adv. Mater.* **27**, 8028–8034 (2015).
27. Yen, T. J. et al. Terahertz magnetic response from artificial. *Mater. Sci.* **303**, 1494–1496 (2004).
28. Paniagua-Domínguez, R., López-Tejiera, F., Marqués, R. & Sánchez-Gil, J. A. Metallo-dielectric core–shell nanospheres as building blocks for optical three-dimensional isotropic negative-index metamaterials. *New J. Phys.* **13**, 123017 (2011).
29. Malassis, L. et al. Topological darkness in self-assembled plasmonic metamaterials. *Adv. Mater.* **26**, 324–330 (2014).
30. Powell, D. A., Shadrivov, I. V. & Kivshar, Y. S. Cut-wire-pair structures as two-dimensional magnetic metamaterials. *Opt. Express* **16**, 15185–15190 (2008).
31. Rill, M. S. et al. Photonic metamaterials by direct laser writing and silver chemical vapour deposition. *Nat. Mater.* **7**, 543–546 (2008).
32. Chang, T. H. P., Mankos, M., Lee, K. Y. & Muray, L. P. Multiple electron-beam lithography. *Microelectron. Eng.* **57**, 117–135 (2001).
33. Burckel, D. B. et al. Fabrication of 3D metamaterial resonators using self-aligned membrane projection lithography. *Adv. Mater.* **22**, 3171–3175 (2010).
34. Gansel, J. K. et al. Gold helix photonic metamaterial as broadband circular polarizer. *Science* **325**, 1513–1515 (2009).
35. Liu, N. et al. Three-dimensional photonic metamaterials at optical frequencies. *Nat. Mater.* **7**, 31–37 (2008).
36. Kim, J. Y. et al. Highly tunable refractive index visible-light metasurface from block copolymer self-assembly. *Nat. Commun.* **7**, 12911 (2016).
37. Kim, B. H. et al. Anomalous rapid defect annihilation in self-assembled nanopatterns by defect melting. *Nano Lett.* **15**, 1190–1196 (2015).
38. Cha, S. K. et al. Au–Ag core–shell nanoparticle array by block copolymer lithography for synergistic broadband plasmonic properties. *ACS Nano* **9**, 5536–5543 (2015).
39. BATES, F. Polymer-polymer phase behavior. *Science* **251**, 898–905 (1991).
40. Xiang, H. et al. From cylinders to helices upon confinement. *Macromolecules* **38**, 1055–1056 (2005).
41. Hou, P., Fan, H. & Jin, Z. Spiral and mesoporous block polymer nanofibers generated in confined nanochannels. *Macromolecules* **48**, 272–278 (2015).
42. Dobriyal, P. et al. Cylindrically confined diblock copolymers. *Macromolecules* **42**, 9082–9088 (2009).
43. Yao, J. et al. Optical negative refraction in bulk metamaterials of nanowires. *Science* **321**, 930–930 (2008).
44. Kabashin, A. et al. Plasmonic nanorod metamaterials for biosensing. *Nat. Mater.* **8**, 867–871 (2009).
45. Lee, D. et al. Arrangement of lamellar microdomains of block copolymer confined in hemispherical cavities having two controlled interfaces. *Macromolecules* **47**, 3997–4003 (2014).
46. Zhu, S., Li, H., Yang, M. & Pang, S. W. High sensitivity plasmonic biosensor based on nanoimprinted quasi 3D nanosquares for cell detection. *Nanotechnology* **27**, 295101 (2016).
47. Lin, H.-Y., Huang, C.-H., Huang, C.-C., Liu, Y.-C. & Chau, L.-K. Multiple resonance fiber-optic sensor with time division multiplexing for multianalyte detection. *Opt. Lett.* **37**, 3969–3971 (2012).
48. Rosman, C. et al. Multiplexed plasmon sensor for rapid label-free analyte detection. *Nano Lett.* **13**, 3243–3247 (2013).
49. Kim, M., & Rho, J. Metamaterials and imaging. *Nano Convergence* **2**, 22 (2015).
50. Fang, N. & Zhang, X. Imaging properties of a metamaterial superlens. *Appl. Phys. Lett.* **82**, 161–163 (2003).
51. Cai, W., Chettiar, U. K., Kildishev, A. V. & Shalaev, V. M. Optical cloaking with metamaterials. *Nat. Photonics* **1**, 224–227 (2007).
52. Sun, J., Zhou, J. & Kang, L. Homogenous isotropic invisible cloak based on geometrical optics. *Opt. Express* **16**, 17768–17773 (2008).
53. Pendry, J. B., Schurig, D. & Smith, D. R. Controlling electromagnetic fields. *Science* **312**, 1780–1782 (2006).
54. Chen, P. Y., Soric, J. & Alù, A. Invisibility and cloaking based on scattering cancellation. *Adv. Mater.* **24**, OP281–OP304 (2012).
55. Jiang, W. et al. Room-temperature broadband quasistatic magnetic cloak. *NPG Asia Mater.* **9**, e341 (2017).
56. Li, A. P., Müller, F., Birner, A., Nielsch, K. & Gösele, U. Fabrication and microstructuring of hexagonally ordered two-dimensional nanopore arrays in anodic alumina. *Adv. Mater.* **11**, 483–487 (1999).
57. Lopes, W. A. & Jaeger, H. M. Hierarchical self-assembly of metal nanostructures on diblock copolymer scaffolds. *Nature* **414**, 735–738 (2001).
58. Johnson, P. B. & Christy, R.-W. Optical constants of the noble metals. *Phys. Rev. B* **6**, 4370 (1972).
59. Kim, S.-W. et al. Thickness-dependent ordering of perpendicularly oriented lamellae in PS-b-PMMA thin films. *Polymer* **74**, 63–69 (2015).
60. Bae, D., Cho, W. J., Jeon, G., Byun, J. & Kim, J. K. Hierarchically well-ordered array of concentric silver nanorings for highly sensitive surface-enhanced raman scattering substrate. *J. Phys. Chem. C* **116**, 26523–26528 (2012).